Improvement of the parabolized stability equation to predict the linear evolution of disturbances in three-dimensional boundary layers based on ray tracing theory

Runjie Song and Lei Zhao

Department of Mechanics, Tianjin University, Tianjin 300072, China

Zhangfeng Huang ⓘ*

Department of Mechanics, Tianjin University, Tianjin 300072, China
and State Key Laboratory of Aerodynamics, China Aerodynamics Research
and Development Center, Mianyang 621000, China

Three-dimensional (3D) boundary layers are common flows in aircraft but present many problems to instability analysis and transition prediction. The difficulties of 3D boundary layers are reviewed and a method is proposed to predict the linear evolution of infinitesimal perturbations in 3D boundary layers, named as RTPSE, in which the line-marching parabolized stability equation (PSE) is improved by applying the ray tracing (RT) theory. Two major improvements are achieved. One is that the marching line is predefined along the direction of group velocity, which is related to both the characteristic line of local dispersion relation and the direction of energy propagation. Another is that the variation of the real part of the spanwise wave number is predicted by RT theory, while its imaginary part is determined based on the conservation relation of generalized growth rate. The implementation of RTPSE for 3D boundary layers is given in detail and involves linear stability theory, the PSE, and RT theory. Both the tracing ray and spanwise wave number are calculated in the real number space, only leading to a second-order error. Direct numerical simulation is performed to verify and validate the prediction by RTPSE in a 3D supersonic boundary layer on a blunt cone with a half angle of $7°$ and an angle of attack of $9°$. Results show that RTPSE can accurately predict the variation of spanwise wave number and linear evolution of disturbances for the whole wave packet, for stationary crossflow waves and for traveling crossflow waves, while the traditional PSE cannot. The application condition of RT theory is investigated numerically, and the caustic does not occur for unstable disturbances, implying that RTPSE is fully applicable to predict the linear evolution of disturbances in 3D boundary layers.

I. INTRODUCTION

Instabilities of laminar flows and the transition of boundary layers have been frequently studied in modern aerodynamic design because of their significant role in drag reduction and thermal protection [1]. Most of the instability theories and their analysis methods are based on two-dimensional (2D) or axisymmetric boundary layers, such as the linear stability theory (LST) [2], parabolized stability equation (PSE) approach [3], and transition prediction e^N method [2]. These

---

*Corresponding author: hzf@tju.edu.cn

theories and methods have been major successes in both theoretical research and engineering applications.

In LST, under the local-parallel-flow assumption, the basic flow $\bar{\mathbf{Q}}$ of 2D boundary layers is only a function of y in the Cartesian system (x, y, z), where x, y, and z are the streamwise, wall-normal, and spanwise directions, respectively. However, it can be perturbed by a small three-dimensional (3D) unsteady disturbance $\mathbf{Q}'(x, y, z, t)$, which can be written in the form of a normal mode [4] as

$$\mathbf{Q}'(x, y, z, t) = \mathbf{q}(y) \exp[i(\alpha x + \beta z - \omega t)] + \text{c.c.,} \tag{1}$$

where ω, α, and β denote the frequency, streamwise wave number, and spanwise wave number, respectively. The vector $\mathbf{q}$ characterizes its shape, $i^2 = -1$, c.c. stands for the complex conjugate, and t stands for the time variable. Because both the basic flow $\bar{\mathbf{Q}}$ and total instantaneous flow $\mathbf{Q} = \bar{\mathbf{Q}} + \mathbf{Q}'$ separately satisfy the Navier-Stokes (NS) equations, the linearized NS equations are derived for $\mathbf{Q}'$, which can be written in the following form:

$$L(\alpha, \beta, \omega; x)\mathbf{q} = \mathbf{0}, \tag{2}$$

where the operator L contains differentiation with respect to y only and the dependence of x is parametric. Equation (2) forms, along with homogenous boundary conditions at the wall and infinity, an eigenvalue problem. In a spatial stability problem, the frequency ω and the spanwise wave number β are usually defined as real values, but the streamwise wave number $\alpha = \alpha_r + i\alpha_i$ is a complex value, where $\sigma = -\alpha_i(\omega, \beta; x)$ represents the spatial growth rate in the x direction. Once $\sigma(\omega, \beta; x)$ is obtained by solving the eigenvalue problem at each location x, the so-called N factor, which measures the accumulated growth of an instability wave with a given ω and β, can be calculated by integrating the growth rate with respect to x along the streamwise direction. Then, transition is deemed to occur when N reaches some critical value N_c in the transition prediction e^N method.

Even for 2D boundary layers, the thickness of the boundary layer increases gradually along the flow direction, leading to the nonparallelism of basic flow. Non-parallel-flow effects on linear instability have often been explained by a perturbative approach suggested by Gaster [5], which is applicable only when nonparallelism causes a small correction to the growth rate, and a nonperturbative approach, free from this restriction, was proposed by Huang and Wu [6]. An alternative and now popular method for studying instabilities in weakly nonparallel flows is the PSE method [3]. For strong nonparallel flows, Huang and Wu [7] proposed a local scattering approach to quantitatively characterize the effect of abrupt changes on instability and transition by a transmission coefficient.

However, most boundary layers are 3D, producing problems for instability analysis and transition prediction. The nonparallelism of basic flow appears both in the streamwise and spanwise directions, while it only exists in the streamwise direction for 2D flows. The nonparallelism of basic flow in the spanwise direction leads to the three dimensionality of flow, which is reflected in three aspects.

(1) The propagation direction of the disturbance is a curve on the wall surface, while it is a straight line for 2D flows.

(2) The perturbation increases in the streamwise direction and in the spanwise direction, namely, β is also a complex value and its imaginary part has the same contribution to the growth rate as that of α, while it is a real value for 2D flows.

(3) β varies along the direction of the disturbance, while the wave number in the spanwise direction can be treated as a constant through an appropriate definition for 2D flows.

For example, the typical wave number $\beta \equiv 2\pi/\lambda$ is defined by the wavelength λ for a 2D flow on a flat plate, and the azimuthal wave number $n \equiv 2\pi/\phi$ is defined by the azimuthal angle ϕ for an axisymmetric flow on a circular cone, even though the typical wave number $\beta = n \times r$ varies with the variation of the cone radius r.

For the first aspect, the results show that group velocity is the propagation velocity of the disturbance energy, so the direction of group velocity is often selected to be the propagation direction of the disturbance for 3D flows. For the second aspect, the growth rate of the disturbance

in 3D flows must be considered. For a disturbance with a specified ω and β_r, the solution of the eigenvalue problem is not unique unless the spanwise growth rate $-\beta_i$ is previously established. Cebeci and Stewartson [8] proposed using a saddle-point condition, i.e., $(\partial\alpha/\partial\beta)_i = 0$, to compute β_i by iterative calculation, which is termed as the SPM and has been widely used to predict the transition of 3D flows [9–11]. However, the SPM overpredicts the amplification ratio of perturbation, because it picks up the local maximum growth rate belonging to different unstable waves instead of a single unstable wave. To eliminate this defect, by using the method of multiple scales, Nayfeh [12] derived a series of partial differential equations to the evolution of amplitude and wave number of the disturbance in a 3D inhomogeneous boundary layer. However, this methodology is too complicated to apply to practical calculations. Song, Zhao, and Huang [13] introduced the concept of generalized growth rate (GGR) and proved that GGR is conservative, and as a result they proposed a more convenient method to calculate GGR by setting $\beta_i = 0$ directly. For the third aspect, the ray tracing (RT) theory [14] in a real number space can well describe the linear evolution of an infinitesimal perturbation in a conservative system. However, boundary layers are not conservative. Therefore, RT theory in a complex number space is required to predict the evolution of wave parameters in 3D boundary layers, leading to a complicated calculation [15]. Zhao *et al.* [16] applied RT theory to the e^N method to predict the evolution of spanwise wave number and the amplitude of a single wave instead of the most unstable wave by the SPM. Although they ignored the imaginary part and applied RT theory only in the real number space directly beyond reason, good improvement can be seen between their results and those by the SPM.

New requirements for the prediction tool of the disturbance evolution are put forward by the three dimensionality. Because of its ability to consider nonparallelism, the PSE has been an excellent tool in predicting the evolution of infinitesimal perturbation in 2D or axisymmetric boundary layers [17–19]. However, the extension of the PSE to 3D boundary layers is not straightforward. Generally, there are three strategies according to different marching methods [20]: (i) the line-marching strategy [21], in which the shape function and α are calculated along a predefined marching line with a given β; (ii) the plane-marching strategy [22,23], in which the 2D shape function and α are solved by marching along the direction in which the basic flow varies slowly (in addition, the basic flow should be periodic in another direction in the 2D cross plane); and (iii) the surface-marching strategy [24], in which the shape function and α are calculated along two adjacent marching lines iteratively and β is determined according to the compatibility relation $\partial\beta_r/\partial x = \partial\alpha_r/\partial z$. A more detailed description of these strategies can be found in the report by Chang [20].

Among the above three strategies, the line-marching PSE is the most frequently applied to 3D inhomogeneous boundary layers. However, two issues still need to be settled: (i) how to predefine the marching line in 3D flows and (ii) how to predetermine the variation of spanwise wave number caused by the inhomogeneity of flow. For a cone with an angle of attack (AoA), Kocian *et al.* [25] proposed the vortex-axis line as the marching line, which is only valid for the stationary crossflow instability and not suitable for traveling crossflow instability or Mack mode instability. For an elliptic cone, Dinzl and Candler [26] used the same strategy to analyze stationary crossflow vortices. In addition, for stationary crossflow instability, Kocian *et al.* [25] determined the variation of spanwise wave number according to the divergence of two adjacent streamlines. Based on an intuitive assumption, they concluded that the variation of spanwise wave number is approximately inversely proportional to the variation of the interval of two streamlines. However, some of their PSE results could not satisfy the DNS results by Balakumar and Owens [27].

In the present paper, by focusing on the difficulties in 3D boundary layers, we improve the line-marching PSE by applying RT theory to predict the linear evolution of different instabilities, e.g., the stationary or traveling crossflow instabilities and/or the Mack mode instability, for 3D boundary layers. The method is denoted as RTPSE for short. The rest of the paper is organized as follows. In Sec. II, we give a general description of stability methods including LST and the PSE, while the improvement method RTPSE is given in detail. In addition, the application condition of RT is also discussed. A brief summary of flow configuration of our interest is given in Sec. III, which

also describes the analysis code used in this paper. In Sec. IV, the evolution of small disturbances performed by DNS is shown, and the validations of the RTPSE results against the DNS results are also presented. Moreover, the application condition of RT is validated numerically. Lastly, we summarize the main conclusions in Sec. V.

II. METHODOLOGY

A. Governing equations for 3D compressible flows

In the present paper, we only focus on the linear evolution of an infinitesimal perturbation which can be described by local (LST) and/or nonlocal (PSE) stability methods for 3D compressible flows. In classical stability methods, the instantaneous flow quantities $\mathbf{Q} = [\rho, u, v, w, T]$ can be decomposed into the steady basic flow and the perturbation quantities in the form of $\mathbf{Q} = \bar{\mathbf{Q}} + \mathbf{Q}'$, where ρ is the density; T is the temperature; and u, v, and w represent the velocity components in the streamwise, wall-normal, and spanwise directions, respectively. The overbar and prime represent the basic flow and the perturbation quantities, respectively. Under the assumption of infinitesimal perturbation, linearized disturbance equations in the orthogonal curvilinear coordinate system can be derived from NS equations and be presented in the compact form

$$
\begin{aligned}
&\mathbf{T}\frac{\partial \mathbf{Q}'}{\partial t} + \mathbf{A}\frac{\partial \mathbf{Q}'}{\partial \xi} + \mathbf{B}\frac{\partial \mathbf{Q}'}{\partial \eta} + \mathbf{C}\frac{\partial \mathbf{Q}'}{\partial \zeta} + \mathbf{D}\mathbf{Q}' \\
&+ \mathbf{V}_{\xi\xi}\frac{\partial^2 \mathbf{Q}'}{\partial \xi^2} + \mathbf{V}_{\eta\eta}\frac{\partial^2 \mathbf{Q}'}{\partial \eta^2} + \mathbf{V}_{\zeta\zeta}\frac{\partial^2 \mathbf{Q}'}{\partial \zeta^2} \\
&+ \mathbf{V}_{\xi\eta}\frac{\partial^2 \mathbf{Q}'}{\partial \xi \eta} + \mathbf{V}_{\xi\zeta}\frac{\partial^2 \mathbf{Q}'}{\partial \xi \zeta} + \mathbf{V}_{\eta\zeta}\frac{\partial^2 \mathbf{Q}'}{\partial \eta \zeta} = \mathbf{0},
\end{aligned} \tag{3}
$$

where ξ, η, and ζ represent the streamwise, wall-normal, and spanwise coordinates, respectively. Coefficient matrices $\mathbf{T}$, $\mathbf{A}$, $\mathbf{B}$, $\mathbf{C}$, $\mathbf{D}$, $\mathbf{V}_{\xi\xi}$, $\mathbf{V}_{\eta\eta}$, $\mathbf{V}_{\zeta\zeta}$, $\mathbf{V}_{\xi\eta}$, $\mathbf{V}_{\xi\zeta}$, and $\mathbf{V}_{\eta\zeta}$ are functions of basic flow quantities and can be found in a study by Oliviero [28]. The streamwise and spanwise curvatures are determined by Eq. (3). In 3D boundary layers, the solution of Eq. (3) can be presented in the following form:

$$
\mathbf{Q}'(\xi, \eta, \zeta, t) = A_0(\xi_0, \zeta_0)\mathbf{q}(\xi, \eta, \zeta)\exp[i\Theta(\xi, \zeta, t)] + \text{c.c.}, \tag{4}
$$

where A_0 is the amplitude of $\mathbf{q}$ at an initial location (ξ_0, ζ_0) and $\mathbf{q}$ represents the shape function normalized by A_0. Θ represents the complex phase, by which the local wave parameters of an unstable wave can be defined:

$$
\omega = -\frac{\partial \Theta}{\partial t}, \quad \alpha = \frac{\partial \Theta}{\partial \xi}, \quad \beta = \frac{\partial \Theta}{\partial \zeta}, \tag{5}
$$

where ω is the radiant frequency and α and β represent the streamwise and spanwise wave numbers, respectively. The boundary layer belongs to a nonconservative system. Therefore, generally, the wave parameters are complex values, and their imaginary parts represent the temporal and spatial growth rates. In addition, the wave parameters ω, α, and β are not independent, but they connect with each other by the following compatibility relation:

$$
\frac{\partial \omega}{\partial \xi} = -\frac{\partial \alpha}{\partial t}, \quad \frac{\partial \omega}{\partial \zeta} = -\frac{\partial \beta}{\partial t}, \quad \frac{\partial \alpha}{\partial \zeta} = \frac{\partial \beta}{\partial \xi}. \tag{6}
$$

By substituting Eqs. (4) and (5) into Eq. (3) with the quasiparallel hypothesis, one can derive the dispersion relation of perturbations with homogeneous boundary conditions without any loss of generality, as

$$
D(\xi, \zeta, t, \alpha, \beta, \omega) = 0, \tag{7}
$$

where D represents the discretized dispersion relation. By substituting the definition of wave parameters in Eq. (5), a first-order partial differential equation for the complex phase function Θ can be presented as

$$D\left(\xi, \zeta, t, \frac{\partial \Theta}{\partial \xi}, \frac{\partial \Theta}{\partial \zeta}, -\frac{\partial \Theta}{\partial t}\right) = 0. \tag{8}$$

B. LST for 3D flows

In LST, under the local-parallel-flow assumption, the disturbance can be written in a normal mode as

$$\mathbf{Q}'(\xi, \eta, \zeta, t) = \mathbf{q}(\eta) \exp[i(\alpha\xi + \beta\zeta - \omega t)] + \text{c.c.}, \tag{9}$$

where the shape function $\mathbf{q}$ is just a function of η. Substituting Eq. (9) into Eq. (3) yields the governing equation for the shape function, which can be written as

$$L(\alpha, \beta, \omega; \xi, \zeta)\mathbf{q}(\eta) = \mathbf{0}, \tag{10}$$

while both the shape function $\mathbf{q}(\eta)$ and the streamwise wave number α can be solved locally at each location (ξ, ζ) with homogenous boundary conditions for a given ω and β.

C. PSE for 3D flows

Unlike LST, in which the solution can be solved locally, PSE needs to be solved by marching downstream. Here, we only present the basic idea of the line-marching PSE, in which the marching line has been selected to be the ξ direction and the flow is homogenous in the ζ direction. By introducing a small parameter ϵ related to the slow variation of a boundary layer and a slow variable $\hat{\xi} = \epsilon\xi$, the perturbation $\mathbf{Q}'$ can be written as [18]

$$\mathbf{Q}'(\xi, \eta, \zeta, t) = A_0(\xi_0, \zeta_0)\mathbf{q}(\hat{\xi}, \eta) \exp\left\{i\left[\int_{\xi_0}^{\xi} \alpha(s)ds + \beta\zeta - \omega t\right]\right\} + \text{c.c.}, \tag{11}$$

where $\mathbf{q}(\hat{\xi}, \eta)$ is the shape function that varies slowly along ξ. Substitution of Eq. (11) into Eq. (3) yields, up to and including $O(\epsilon)$, the equation

$$\hat{\mathbf{A}}\frac{\partial \mathbf{q}}{\partial \xi} + \hat{\mathbf{B}}\frac{\partial \mathbf{q}}{\partial \eta} + \hat{\mathbf{D}}\mathbf{q} + \hat{\mathbf{V}}_{\eta\eta}\frac{\partial^2 \mathbf{q}}{\partial \eta^2} = \mathbf{0}, \tag{12}$$

through which the shape function $\mathbf{q}$ and wave number α can be solved numerically by a marching process along ξ with homogeneous boundary conditions for a given ω and β. Different from the usual PSE, which is derived in the Cartesian coordinate system, the current PSE is derived in the orthogonal curvilinear coordinate system and the curvature is considered. A more comprehensive description of the coefficient matrices and the numerical method can be found in the report by Oliviero [28].

D. RT theory for 3D flows

According to the method of characteristics, the dispersion relation Eq. (8) can be solved by introducing a free parameter σ, as follows [29]:

$$\frac{d\xi}{d\sigma} = \frac{\partial D}{\partial \alpha}, \quad \frac{d\zeta}{d\sigma} = \frac{\partial D}{\partial \beta}, \quad \frac{dt}{d\sigma} = -\frac{\partial D}{\partial \omega}, \quad \frac{d\alpha}{d\sigma} = \frac{\partial D}{\partial \xi}$$

$$\frac{d\beta}{d\sigma} = \frac{\partial D}{\partial \zeta}, \quad \frac{d\omega}{d\sigma} = \frac{\partial D}{\partial t}, \quad \frac{d\Theta}{d\sigma} = \frac{\partial D}{\partial \alpha}\alpha + \frac{\partial D}{\partial \beta}\beta + \frac{\partial D}{\partial \omega}\omega, \tag{13}$$

where the solution is a curve in the six-dimensional space $(\xi, \zeta, t, \alpha, \beta, \omega)$, which is presented as functions of the free parameter σ. If an initial condition $(\xi_0, \zeta_0, t_0, \alpha_0, \beta_0, \omega_0)$ is given, the solution

of an initial value problem (IVP) can be solved. If the boundary conditions at the initial position (ξ_0, ζ_0, t_0) and the final position (ξ_1, ζ_1, t_1) are given, the solutions of a boundary value problem (BVP) can be also solved.

Based on the solution in Eq. (13) and the dispersion relation in Eq. (8), it is easy to obtain

$$
\frac{d\xi}{dt} = \frac{d\xi}{d\sigma} \bigg/ \frac{dt}{d\sigma} = -\frac{\partial D}{\partial \alpha} \bigg/ \frac{\partial D}{\partial \omega} = \frac{\partial \omega}{\partial \alpha} \equiv u_{g\xi}
$$

$$
\frac{d\zeta}{dt} = \frac{d\zeta}{d\sigma} \bigg/ \frac{dt}{d\sigma} = -\frac{\partial D}{\partial \beta} \bigg/ \frac{\partial D}{\partial \omega} = \frac{\partial \omega}{\partial \beta} \equiv u_{g\zeta}
$$

$$
\tan(\theta) \equiv \frac{d\zeta}{d\xi} = \frac{d\zeta}{d\sigma} \bigg/ \frac{d\xi}{d\sigma} = \frac{\partial D}{\partial \beta} \bigg/ \frac{\partial D}{\partial \alpha} = -\frac{\partial \alpha}{\partial \beta} = \frac{u_{g\zeta}}{u_{g\xi}}, \tag{14}
$$

where $\mathbf{u}_g = (u_{g\xi}, u_{g\zeta}) \equiv (\partial \omega / \partial \alpha, \partial \omega / \partial \beta)$ is defined as the local group velocity of the wave and θ is the direction angle of group velocity. Equation (14) implies that the group velocity is related to the characteristic line, and the integral result of this equation constitutes a ray the tangent direction of which at each position is the same as that of the group velocity. Because the local group velocity is the propagation velocity of the perturbation energy in physics [30], the direction of the group velocity represents the propagation direction of perturbation, and the ray can be treated as the marching line in the line-marching PSE.

Generally, the rays are complex for 3D flows, so the integration in Eq. (14) should be in the complex number space, producing many inconveniences. For example, the calculation requires the basic flow to be known in the complex number space [15]. These inconveniences can be avoided at the cost of an additional approximation by moving the whole path from the complex number space to the real number space.

For a steady 3D boundary layer, which is the focus of attention in this paper, the phase function Θ can be presented by two given locations (ξ_0, ζ_0, t_0) and (ξ_1, ζ_1, t_1), as

$$
\Theta = \int_{\xi_0}^{\xi_1} \alpha d\xi + \int_{\zeta_0}^{\zeta_1} \beta d\zeta - \int_{t_0}^{t_1} \omega dt = \int_{\xi_0}^{\xi_1} \left(\alpha + \beta \frac{d\zeta}{d\xi} \right) d\xi - \text{const}, \tag{15}
$$

in which the last term is a constant because the frequency ω of the disturbance is a real constant when the disturbance evolves in a steady 3D boundary layer. If the two locations (ξ_0, ζ_0, t_0) and (ξ_1, ζ_1, t_1) are located in a ray that is determined by Eq. (14), we consider a variation of the path of the form $\zeta \to \zeta + \delta\zeta$ and $\beta \to \beta + \delta\beta$, where $\delta\zeta(\xi_0) = \delta\zeta(\xi_1) = 0$ without any loss of generality. Then the first variation of Eq. (15) can be written as

$$
\delta\Theta = \int_{\xi_0}^{\xi_1} \left[\frac{\partial \alpha}{\partial \beta} \delta\beta + \frac{\partial \alpha}{\partial \zeta} \delta\zeta + \delta\beta \frac{d\zeta}{d\xi} + \beta \delta\left(\frac{d\zeta}{d\xi} \right) \right] d\xi. \tag{16}
$$

For the last term in Eq.(16), integration by parts can be performed to obtain

$$
\delta\Theta = \int_{\xi_0}^{\xi_1} \left[\left(\frac{\partial \alpha}{\partial \zeta} - \frac{\partial \beta}{\partial \xi} \right) \delta\zeta + \left(\frac{\partial \alpha}{\partial \beta} + \frac{d\zeta}{d\xi} \right) \delta\beta \right] d\xi + (\beta \delta\zeta)_{\xi_0}^{\xi_1} = 0, \tag{17}
$$

in which the first variation is zero according to Eqs. (6) and (14), and the last term is also zero because the variation of ζ is zero at the bounds of the integral. In optics, this result is known as Fermat's principle, which states that the optical path passing through two given points is an extremum.

This property allows us to replace the complex path with a real path by taking $\delta\zeta = -i\zeta_i$ in Eq. (16), which only leads to a second-order error on the phase function Θ. The results show that using real rays only introduces an error of 0.1% but greatly improves computational efficiency [15].

The analysis of the modified ray is

$$\frac{d\zeta}{d\xi} = \frac{u_{g\zeta}}{u_{g\xi}} = \left(\frac{u_{g\zeta}}{u_{g\xi}}\right)_r \{1 + O[(u_{g\xi})_i(u_{g\eta})_i]\} \approx \left(\frac{u_{g\zeta}}{u_{g\xi}}\right)_r, \tag{18}$$

where the imaginary parts of the group velocity $\mathbf{u}_g$ are omitted because they are much smaller than their real parts. Then, by integrating Eq. (14) and omitting the imaginary parts, we can obtain the governing equation of rays in the real number space, as

$$\xi_1 = \xi_0 + \int_{t_0}^{t_1} (u_{g\xi})_r dt$$

$$\zeta_1 = \zeta_0 + \int_{t_0}^{t_1} (u_{g\zeta})_r dt$$

$$t_1 = t_0 + dt$$

$$\theta = \arctan\left[\left(\frac{u_{g\zeta}}{u_{g\xi}}\right)_r\right]. \tag{19}$$

Except for the predefinition of marching rays in Eq. (19), the predetermination of β is also required by the line-marching PSE. Fortunately, the method of characteristics is also applicable for β.

On the one hand, the solution in Eq. (13) also implies that the variation of β is governed by

$$\frac{d\beta}{dt} = \frac{d\beta}{d\sigma} \Big/ \frac{dt}{d\sigma} = -\frac{\partial D}{\partial \zeta} \Big/ \frac{\partial D}{\partial \omega}. \tag{20}$$

On the other hand, according to the definition of the total differential, we have

$$\frac{d\beta}{d\sigma} = \frac{\partial \beta}{\partial \xi}\frac{d\xi}{d\sigma} + \frac{\partial \beta}{\partial \zeta}\frac{d\zeta}{d\sigma} + \frac{\partial \beta}{\partial t}\frac{dt}{d\sigma}. \tag{21}$$

Substitution Eqs. (21) and (14) into Eq. (20) yields

$$\frac{d\beta}{dt} = \frac{\partial \beta}{\partial t} + u_{g\xi}\frac{\partial \beta}{\partial \xi} + u_{g\zeta}\frac{\partial \beta}{\partial \zeta} = -\frac{\partial D}{\partial \zeta} \Big/ \frac{\partial D}{\partial \omega}, \tag{22}$$

where $d/dt = \partial/\partial t + u_{g\xi}\partial/\partial \xi + u_{g\zeta}\partial/\partial \zeta$ is the material derivative along the group velocity, indicating that the variation of β governed by Eq. (22) is also along the direction of group velocity. Similarly, β can be obtained by integrating Eq. (22) along a ray in the real number space, as

$$(\beta_1)_r = (\beta_0)_r - \int_{t_0}^{t_1} \left(\frac{\partial D}{\partial \zeta} \Big/ \frac{\partial D}{\partial \omega}\right)_r dt. \tag{23}$$

As mentioned previously, both the IVP and BVP can be solved numerically. If the wave parameters of the disturbance in the initial position are given, the variation of β_r can be predicted by solving Eq. (23), while the imaginary part β_i can be set to be zero according to the conservation relation of GGR [13].

E. Application condition of RT for 3D flows

The only application condition of RT theory is away from caustics with the caustics condition

$$\Delta = \left[\left(\frac{\partial^2 \omega}{\partial \alpha \partial \beta}\right)^2 - \frac{\partial^2 \omega}{\partial \alpha^2}\frac{\partial^2 \omega}{\partial \beta^2}\right]^{1/2} = 0. \tag{24}$$

While the RT theory breaks down near caustics, this situation can be addressed mathematically by using the concept of the Airy integral [14]. However, this process is very complicated for 3D

TABLE I. Review of the difficulties of 3D boundary layers and their strategies.

Classification	Difficulty	Strategy	Remark
Nonparallelism	Nonparallelism effect	PSE	Line-marching PSE [21]
	Propagation direction	θ by Eq. (19)	RT theory
Three dimensionality	Determination of β_i	$\beta_i = 0$	GGR conservation [13]
	Variation of β_r	β_r by Eq. (23)	RT theory
Line-marching PSE	Definition of marching path	Ray by Eq. (19)	RT theory
	Prediction of β_r	β_r by Eq. (23)	RT theory

boundary layers, and it is unnecessary if a caustic does not occur. The existence of caustics is usually checked numerically. For incompressible boundary layers, caustics are not found because the condition $\Delta = 0$ does not occur [31–33]. For 3D compressible boundary layers when the Mach number is high, the existence or absence of caustics is still uncertain. Therefore, a conservative option is to validate the condition for whole locations and wave parameters, leading to a huge calculation. Fortunately, most disturbances considered in this paper are unstable, so we only validate this condition for unstable disturbances in Sec. IV.

F. RTPSE for 3D flows

As mentioned in Sec. I, the difficulty in extending the PSE to 3D flows includes two aspects: predefining the marching path and predicting the variation of the spanwise wave number. By introducing RT theory, these two difficulties have been overcome, in which the former is predefined by Eq. (19) and the latter is determined by Eq. (23) in the real number space.

Based on the RT theory, we improve the line-marching PSE to predict the linear evolution of the disturbance in 3D boundary layers, which is denoted as RTPSE. Its computation strategy is as follows:

(i) Specify ω_0 and β_0 at an initial location (ξ_0, ζ_0, t_0), and obtain the corresponding α_0 by solving Eq. (10) through LST.

(ii) Solve Eq. (10) by LST to calculate the local group velocity $\mathbf{u}_g = (u_{g\xi}, u_{g\zeta})$, and obtain the partial derivatives $\partial D/\partial \zeta$ and $\partial D/\partial \omega$ for a given $(\alpha_0, \beta_0, \omega_0)$ at location (ξ_0, ζ_0, t_0) with the assistance of Eq. (7).

(iii) Solve Eq. (19) by RT to obtain the next position (ξ_1, ζ_1, t_1) with a proper $dt = c_t \times \min(\Delta\xi/u_{g\xi}, \Delta\zeta/u_{g\zeta})$ in the real number space, and obtain β_1 by Eq. (23), while $\omega_1 = \omega_0$ because of the steady characteristics of basic flow, where $\Delta\xi$ and $\Delta\zeta$ are the mesh spacings in the ξ and ζ directions, respectively, and $c_t \in (0, 1)$ is the coefficient.

(iv) Extract the basic flow at the next position (ξ_1, ζ_1, t_1) on the ray started from (ξ_0, ζ_0, t_0) and adjust the streamwise velocity $\bar{u}$ pointing to the direction of group velocity and adapt the spanwise velocity $\bar{w}$ perpendicular to it.

(v) Perform the line-marching PSE by solving Eq. (12) at two positions (ξ_0, ζ_0, t_0) and (ξ_1, ζ_1, t_1) to calculate the shape function, amplitude ratio, and modified streamwise wave number at location (ξ_1, ζ_1, t_1), where the marching line is along the ray and β is updated in advance.

(vi) Replace position (ξ_1, ζ_1, t_1) to be (ξ_0, ζ_0, t_0) and repeat steps (ii) to (v) to obtain the solution for all positions in the rays.

Now, we review the difficulties of 3D boundary layers mentioned in Sec. I. The difficulties and their corresponding strategies are summarized in Table I, and the table shows that all of the difficulties have been addressed with our method based on RT theory, the line-marching PSE [21], and GGR conservation [13], implying that the evolution of the disturbance in 3D boundary layers can be predicted by the method.

The results also show that there are no restrictions (except for the caustics that would not occur), implying that the method, RTPSE, can be applied to predict the linear evolution for various
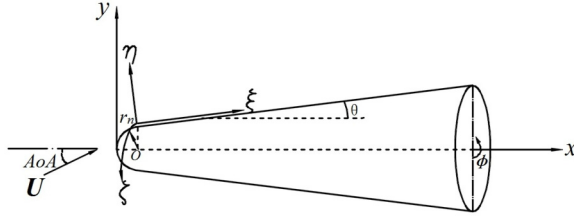
FIG. 1. Schematic of a blunt cone with an AoA.

instabilities, such as the stationary or traveling crossflow instability and the first or second Mack mode instability for 3D and/or 2D compressible and/or incompressible steady flows.

III. NUMERICAL METHOD

A. Basic flow simulation and code validation

To verify and validate the reliability of RTPSE, we select the model and free-stream conditions from Ref. [34], which is suitable to study the stationary and traveling crossflow instabilities. Figure 1 shows the computational model for hypersonic flow over a blunt cone, which has a nose radius $r_n = 1.6$ mm, length $L = 0.704$ m, half angle $\theta = 7°$, and AoA $= 9°$. The free-stream conditions correspond to a free-stream Mach number Ma $= 7.07$, unit Reynolds number Re$_\infty = 9.5 \times 10^6$ m^{-1}, and free-stream temperature $T_\infty = 54.56$ K, while the temperature at the wall is $T_w = 310$ K.

The basic flow is obtained by using an in-house NS solver developed and used by Zhao *et al.* [35,36]. The convection terms are split by using a Steger-Warming splitting method and discretized with a third-order weighted essentially nonoscillatory scheme [37], whereas the viscous terms are discretized with a fourth-order center finite difference scheme. A third-order Runge-Kutta method with total variation diminishing characteristics is used for time advance.

To validate our code, we simulated the steady flow over a blunt cone without and with an AoA. The 2D flow with zero AoA was simulated by Zhong and Ma [38] using their high-order shock-fit method and the 3D flow with 6° AoA was given by Balakumar and Owens [27]. Figure 2 shows the comparison of basic flows between our DNS results and others. The results show that there is good agreement between our result and Zhong and Ma's and Balakumar and Owens's results, implying the validation of our code.

To check the grid independence, five kinds of mesh distribution are used to simulate the basic flow over a blunt cone with 9° AoA, as shown in Table II, in which the middle grid has an equivalence mesh count with other researchers who performed simulations on a cone with an AoA [21,39].
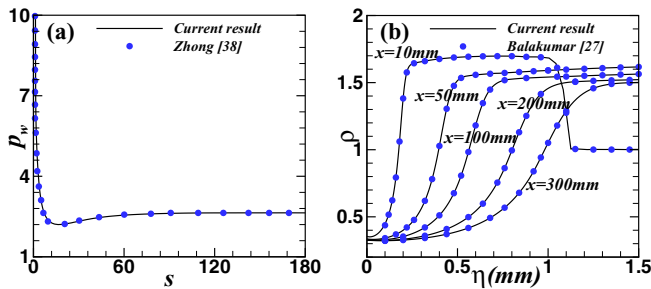

FIG. 2. Validation of DNS: (a) pressure at the wall for 2D flow compared with Zhong and Ma [38] and (b) density along the wall-normal direction for 3D flow compared with Balakumar and Owens [27].

TABLE II. Different density meshes for the validation of grid independence.

Grid	Mesh size ($\times 10^6$)	ξ	η	ζ
Tiny	8	301	141	181
Coarse	11	301	181	201
Medium	29	601	201	241
Fine	51	601	281	301
Extra fine	130	801	361	451

Because of the azimuthal symmetry of the boundary layer about the windward and leeward planes, only half of a cone is selected in the computation of basic flow. Figure 3(a) shows the effect of grid resolution on the basic flow, and the the figure shows that the profiles of streamwise velocity and temperature are overlapped among the medium, fine, and extra fine grids, while the profiles of the coarse and tiny grids near the outer edge of the boundary layer begin to deviate. The difference of basic flow leads to the variation of flow instability characteristics, so the effect of grid resolution on the growth rate of most unstable stationary crossflow waves is also considered. As shown in Fig. 3(b), the growth rate converges to a constant as the number of grids increases, and the relative errors of growth rate compared with those of the extra fine grid are 5.92% (tiny), 2.59% (coarse), 0.66% (medium), and 0.21% (fine), respectively, implying that the mesh size of the medium and fine grids is sufficient within a certain range of accuracy.

B. Disturbance simulation and boundary conditions

To verify and validate the reliability of RTPSE, DNS was also performed. Different from the DNS of basic flow, in which the nose and head shock are included in the computation domain and only a half model was simulated, we selected the computation domain as one part of the basic flow but selected a full model to perform DNS to predict the linear evolution of the disturbances. As shown in Fig. 4(a), the computation domain started at $x = 93$ mm where it is near the neutral curve for the crossflow instability. To avoid the interaction of unstable waves with the stream vortex on the leeward of the cone, the computational domain was set to end at $x = 270$ mm. The length of computation domain in the axial direction is relatively short, but there are about ten wavelengths of disturbances, which is long enough to study in this paper. For a stationary crossflow, the streamwise wavelength along the vortex direction approaches infinity. But the axial direction does not align with the vortex direction for the flow on a cone with an AoA, which manifests as the alternate appearance of high-speed and low-speed streaks in the axial direction, leading to the wave form of the stationary crossflow in the axial direction, as shown in Fig. 5.
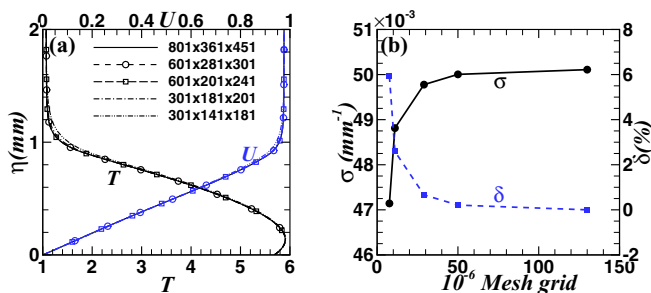

FIG. 3. Effect of grid resolution on (a) the basic flow and (b) the growth rate of the most unstable stationary crossflow wave at $x = 187$ mm, $\phi = 90°$, where ϕ denotes the azimuthal angle. The relative error is defined as $\delta = (\sigma_e - \sigma)/\sigma_e \times 100$, where σ_e is the growth rate of the extra fine grid.
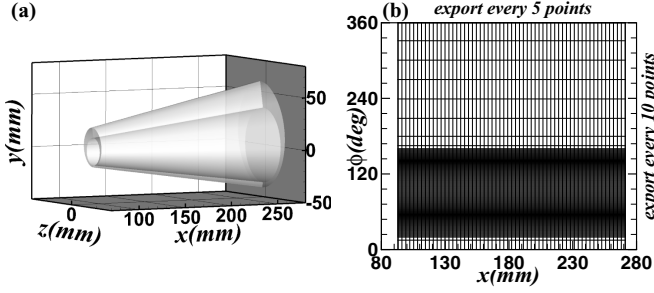
FIG. 4. Sketch map of the (a) computation domain and (b) computation mesh in the x-ϕ plane for disturbance simulation.

The upper boundary of the computation domain is chosen to exclude the head shock in order to apply high-order finite difference schemes. Specifically, the convection terms are discretized with a fifth-order upwind finite difference scheme, and the viscous terms are discretized with a sixth-order center finite difference scheme.

At the inlet, a small disturbance is introduced as

$$\mathbf{Q}'(\eta, \phi, t) = A_0 \mathbf{q}(\eta) \exp[i(n_0 \phi - \omega t)] + \text{c.c.}, \tag{25}$$

where A_0 is the initial amplitude of 10^{-8}, $n_0 = \beta_0 \times r_0$ is the azimuthal wave number (number of waves), r_0 is the local radius of the blunt cone at the inlet, β is the local spanwise wave number, and $\mathbf{q}$ represents the shape function obtained by LST at the inlet with a given $\phi_c = 25°$. Based on the prediction of β in Eq. (23), it is easy to obtain the prediction of n, as

$$(n_1)_r = (n_0)_r - \int_{t_0}^{t_1} \left(\frac{\partial D}{\partial \phi} \bigg/ \frac{\partial D}{\partial \omega} \right)_r dt, \tag{26}$$

where $n = \beta \times r$ and r is the local radius of the blunt cone. At the outlet, an artificial boundary condition is specified by introducing a fringe sponge region [40,41] to dampen the disturbance from $x = 240$ to 270 mm. A nonslip isothermal boundary condition is applied at the wall, and a nonreflecting boundary condition is adapted at the upper region.

The total grid point for disturbance DNS is up to 60×10^6. The computation domain in the circumferential direction is selected to be a full model but with a nonuniform distributed mesh with 1001 points. Because the crossflow instability mainly exists in the area of $\phi = 20°$–$160°$, the mesh in this area is refined to ensure that each unstable wave has more than 30 points in one wavelength, but in the other region the mesh is gradually coarsened, as shown in Fig. 4(b), which helps to minimize
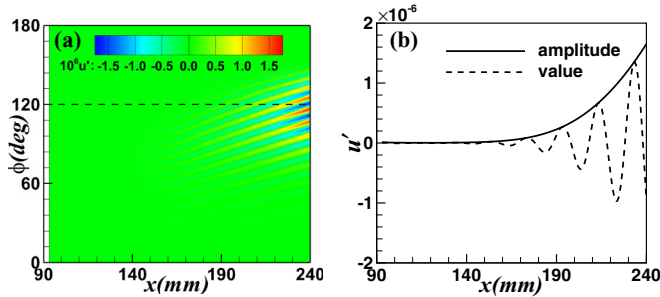

FIG. 5. Wave form of the stationary crossflow wave in the axial direction. (a) Contours of u'. (b) Value of u' (dashed line) and its amplitude (solid line) at $\phi = 120°$.
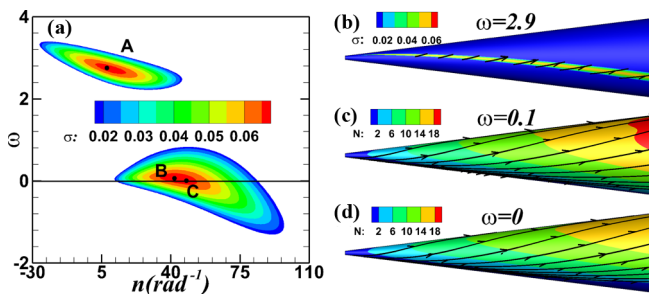
FIG. 6. Instability analysis and N-factor distribution: (a) growth rate distribution in the n-ω plane at $x = 195$ mm, $\phi = 105°$; (b) growth rate distribution for the second Mack mode instability with high frequency $\omega = 2.9$; (c) N-factor distribution for the traveling crossflow instability with low frequency $\omega = 0.1$; and (d) N-factor distribution for the stationary crossflow instability with zero frequency $\omega = 0$. The line in (b)–(d) is the integral line or marching line the direction of which is in the direction of the group velocity.

the computation cost. The mesh in the axial direction is uniform and there are at least 30 points per wavelength of unstable disturbances. The mesh in the wall-normal direction is nonuniform to match the distribution of the boundary layer and there are more than 100 points in the boundary layer. The convergence study of the disturbance DNS has been performed by doubling the grid number in each direction separately and the results are in good agreement with each other.

IV. RESULTS AND DISCUSSION

In this section, the linear evolution of disturbances, including stationary and traveling crossflow waves, is calculated by DNS and RTPSE, and the results are compared to verify and validate the reliability of RTPSE. Then, a short discussion regarding the application condition of RT is performed.

A. Instability analysis of basic flow

Figure 6 shows the result of the instability analysis of basic flow. Figure 6(a), which presents the growth rate distribution in the n-ω plane at $x = 195$ mm and $\phi = 105°$, shows there are two typical unstable areas indicating the growth rate is larger than zero. Disturbances in the unstable area with a high frequency belong to the second Mack mode instability, the most unstable wave of which is marked as label A near $\omega = 2.9$, while perturbations in the unstable area with a low frequency are classified as the first Mack mode instability. Because of the existence of crossflow, the unstable areas are no longer symmetric with respect to the axis $n = 0$. The unstable area with a low frequency intersects with the axis $\omega = 0$, leading to the appearance of crossflow instability. The most unstable wave is marked as label B near $\omega = 0.1$, which is called the traveling crossflow wave, while the most unstable wave with $\omega = 0$, which is marked as label C, belongs to the stationary crossflow wave. As shown in Fig. 6(b), while the growth rates belonging to the second Mack mode instability with a high frequency $\omega = 2.9$ are bigger, its unstable area on the cone is narrow and intersects with the integral line or the marching line in a short distance, leading to an integral result N that is less than 2. Therefore, the second Mack mode instability is not important in this case. However, the unstable areas for the stationary crossflow instability with zero frequency $\omega = 0$ and for the traveling crossflow instability with low frequency $\omega = 0.1$ intersect with the integral line after traveling for a long distance, resulting in a very large N, as shown in Figs. 6(c) and 6(d). Therefore, both the stationary and traveling crossflow instabilities play a key role in the transition process, and they are selected to verify and validate the reliability of RTPSE.
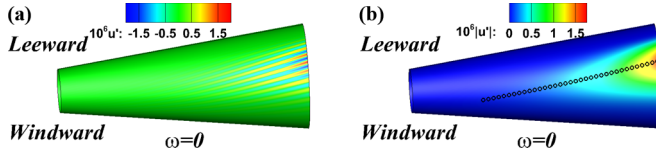
FIG. 7. DNS result of the stationary crossflow wave: (a) contour of the peak value in the wall-normal direction of u' and (b) contour of the amplitude of u'. The symbols represent the location of the hump of the amplitude in the spanwise direction.

B. Stationary crossflow instability

The linear evolution of the stationary crossflow wave with $\omega = 0$, $n = 65$, and $A_0 = 10^{-8}$ is simulated by DNS. Figure 7(a) shows the contour of the peak value in the wall-normal direction of u', and the figure shows that disturbances grow gradually from upstream to downstream within a certain range of ϕ and there are obvious ribbon structures manifesting that positive u' appears alternately with negative u'. Because of the stationary characteristics, the amplitude in each location needs to be extracted by interpolation among the peaks of the disturbance, which is shown in Fig. 7(b). The figure shows that most of the energy mainly exists in a certain region of ϕ and that the peak value in the azimuthal direction shifts gradually from the windward to the leeward as disturbances propagate from upstream to downstream.

Figure 8 shows the distribution of u' at four locations. At inlet $x = 93$ mm, a disturbance with uniform amplitude $A_0 = 10^{-8}$ is set along the circumferential direction in the form of Eq. (25). Because crossflow near the windward and the leeward is weak, stationary crossflow waves are stable near the windward $\phi = 0°$ and the leeward $\phi = 180°$, and are only unstable within a certain range of ϕ. The amplitude of the imposed disturbance decays rapidly near the windward and the leeward but increases gradually within a certain range of ϕ as it propagates from upstream to downstream, leading to a wave packet, in which the location ϕ_p of the wave crest shifts and the azimuthal wave number n varies. However, because the frequency of the initial disturbance imposed at the inlet is
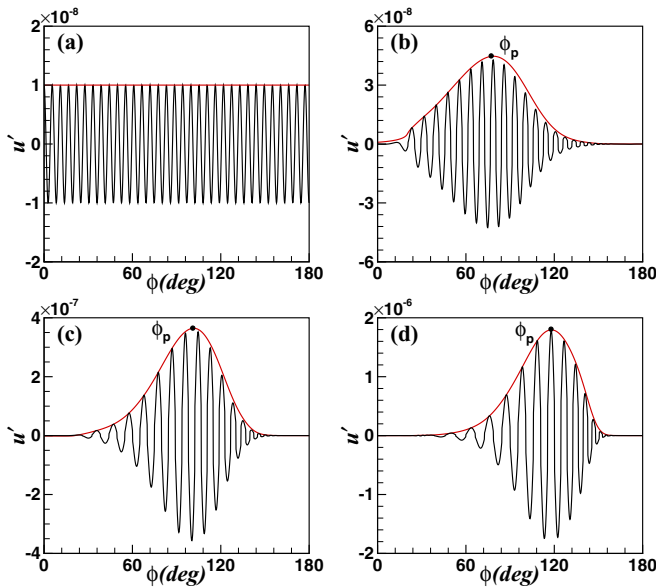

FIG. 8. Distribution of u' at different locations obtained by DNS: (a) $x = 93$ mm, (b) $x = 140$ mm, (c) $x = 190$ mm, and (d) $x = 240$ mm. ϕ_p is the location of the hump of the wave packet.
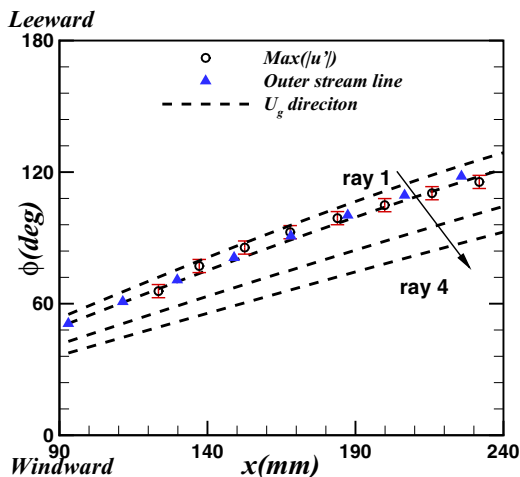
FIG. 9. Comparison of the disturbance evolution paths between DNS, RT, and the outer streamline for stationary crossflow waves. Circle symbols: position of the wave crest in the spanwise direction. Triangle symbols: the outer streamline. Dashed lines: tracing rays starting from different points at the inlet.

zero, u' in the spanwise direction at each location does not change as it propagates from upstream to downstream, leading to a stationary wave packet.

Figure 9 presents the evolution path of the stationary crossflow wave obtained by DNS and RT. Based on DNS, because the amplitude of the disturbance in each wave packet reaches its maximum value in the spanwise direction at the ϕ_p location, the curve constituted by the points of ϕ_p at different x values usually represents the evolution path of the disturbance. Because of the stationary characteristics of the wave packet, the value of ϕ_p obtained by the hump location of each wave would be slightly different for different interpolation schemes, so the error bar for each location is also given in Fig. 9. The tracing ray can be obtained by Eq. (19) for a given start point (ξ_0, ζ_0) at the inlet, which presents the evolution path of the disturbance according to RT theory. Four tracing rays along the group velocity direction are shown in Fig. 9, in which good agreement can be seen between the tracing ray 2 by RT and the evolution path by DNS, indicating that it is reliable to select the tracing ray along the group velocity to analyze the evolution of the disturbance. The outer streamline is also given in Fig. 9, and the streamline is close to the evolution path by DNS, indicating that the outer streamline is a good approximation.

It should be noted that most people only verify or validate the result along the evolution path by DNS in Fig. 9. However, as shown in Fig. 8, disturbances propagate downward in the form of a wave packet in the spanwise direction. In addition, the evolution path by DNS may be treated as the most dangerous evolution path of the wave packet but does represent all waves in the wave packet. To verify and validate the reliability of RTPSE for the whole wave packet, four tracing rays were considered. Ray 2 is along the location of the peak value of the wave packet, ray 1 is on the steep slope of the wave packet closest to the leeward side, while rays 3 and 4 are on the gentle slope of the wave packet closest to the windward side. These results along four tracing rays reflect the evolution of the whole wave packet.

Figure 10 shows the comparison of the azimuthal wave number n obtained by DNS with that by RT along four tracing rays for the stationary crossflow wave. The azimuthal wave number n of DNS is calculated according to the hump location of each wave in the wave packet, and error bars exist because of the stationary characteristic of the wave packet, which is also presented in Fig. 10. The azimuthal wave number n is predicted by RT by Eq. (26); however, it remains a constant in the traditional PSE. Figure 10 shows that the azimuthal wave number n does vary and that its variation can be satisfactorily predicted by RTPSE and DNS.
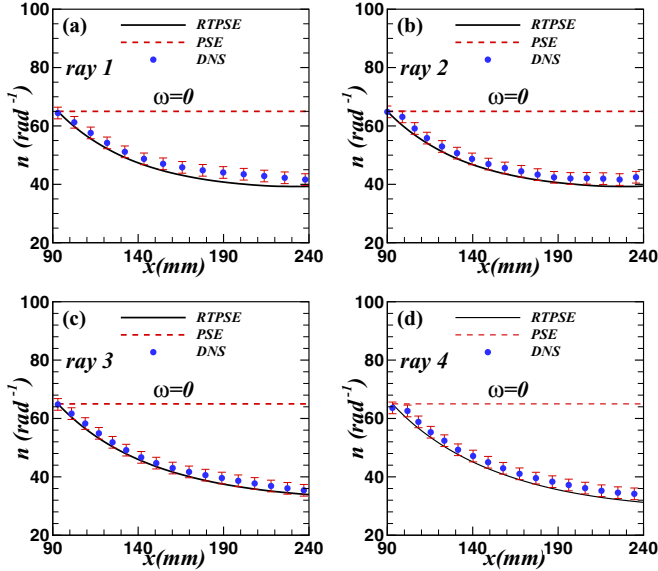
FIG. 10. Comparison of the azimuthal wave number n among RTPSE, PSE, and DNS for stationary crossflow waves: (a) ray 1, (b) ray 2, (c) ray 3, and (d) ray 4.

Figure 11 shows the comparison of the amplitude ratio among RTPSE, PSE, and DNS along four tracing rays for stationary crossflow waves. At the inlet, the shape function **q** in Eq. (25) is obtained by LST with a given ϕ_c but imposed at the inlet for all ϕ. Because of the nonlocal characteristics, disturbances introduced at the inlet undergo a modulation process before they grow or decay exponentially, so we compared the amplitude ratios starting at $x = 110$ mm after the modulation instead of at the inlet $x = 93$ mm. The amplitude ratio by DNS is interpolated
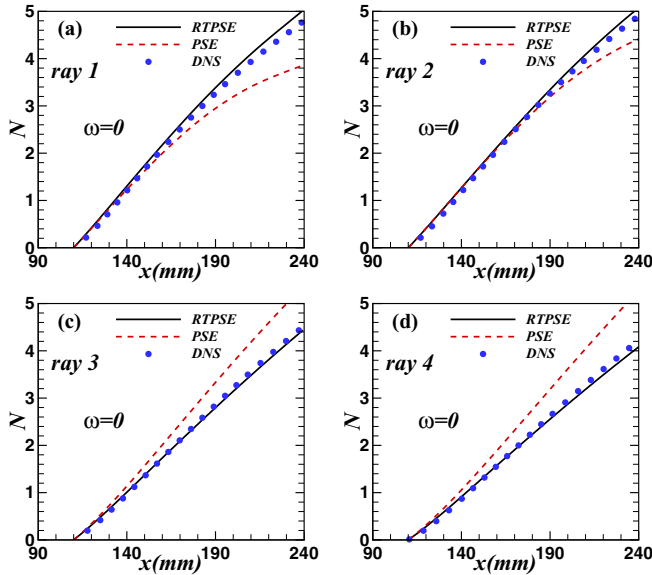
FIG. 11. Comparison of the amplitude ratio $N = \ln(A/A_{x=110})$ among RTPSE, PSE, and DNS for stationary crossflow waves: (a) ray 1, (b) ray 2, (c) ray 3, and (d) ray 4.
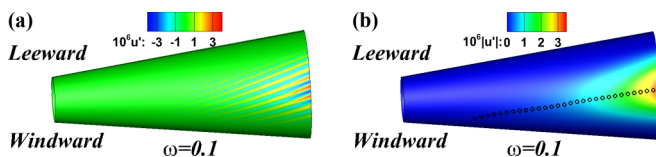
FIG. 12. DNS result of traveling crossflow waves: (a) transient contour of the peak value in the wall-normal direction of u' and (b) contour of the amplitude of u'. The symbols represent the location of the hump of amplitude in the spanwise direction.

according to the hump amplitude of each wave in the wave packet, which may produce some errors in the amplitude evolution. The results show that the amplitude predicted by RTPSE presents satisfactory prediction results, while the PSE is obviously deviated from DNS. It is worth noting that, because the axial direction does not align with the vortex direction, crossflow waves manifest as the alternately high-speed and low-speed streaks in the axial direction. Figure 5(b) shows that the short distance $\Delta x = 147$ mm contains no more than eight wavelengths in the axial direction, and the computational domain is close to the head of the blunt cone, so the deviation of the amplitudes between the PSE and RTPSE would be large and could not be accepted any more for a long distance downstream.

Differing from the method proposed by Dinzl and Candler [26] in which the vortex-axis line is selected as the marching line and stationary crossflow waves along it can be satisfactorily predicted, RTPSE can predict both the spanwise wave number and linear amplification ratio of stationary crossflow waves for all tracing lines. Furthermore, the next subsection shows that the method can also predict the evolution of traveling crossflow waves, while the former cannot.

C. Traveling crossflow instability

The simulation of linear evolution for a traveling crossflow wave by DNS was similar to that for a stationary crossflow wave except for the frequency in which the frequency for the former is $\omega = 0.1$ (or $f = 16.66$ kHz). In the same way, the disturbance distribution, evolution path prediction, spanwise number variation, and amplitude comparison of traveling crossflow waves are analyzed in detail. Although the envelope of the wave packet does not change, the hump of
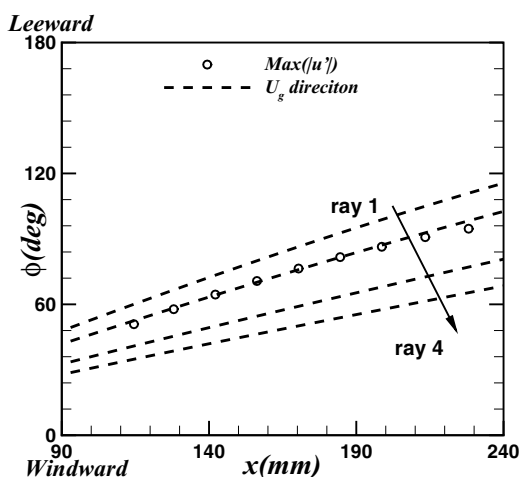

FIG. 13. Comparison of the disturbance evolution path between DNS and RT for traveling crossflow waves. Circle symbols: position of the wave crest in the spanwise direction. Dashed lines: path along group velocity from different starts.
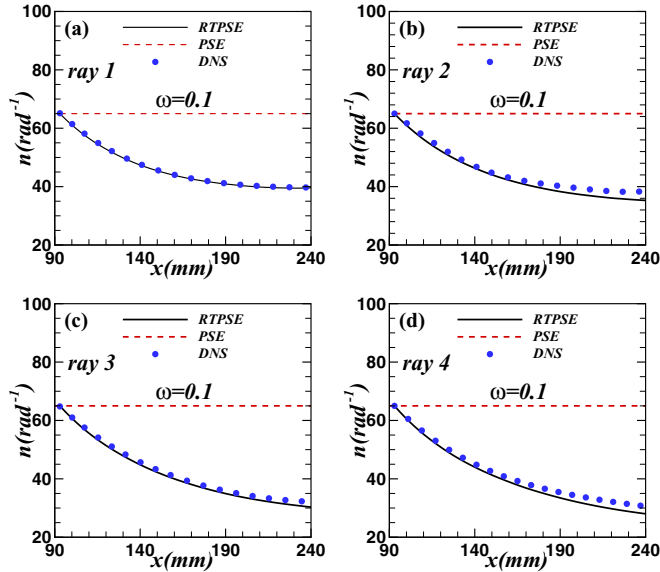
FIG. 14. Comparison of the azimuthal wave number n among RTPSE, PSE, and DNS for traveling crossflow waves: (a) ray 1, (b) ray 2, (c) ray 3, and (d) ray 4.

each wave in the wave packet shifts in the spanwise direction because of a nonzero frequency of initial disturbances imposed at the inlet, resulting in the evolution path, spanwise wave number, and amplitude of traveling crossflow waves being precisely obtained by DNS. However, an interpolation operation is required for stationary crossflow waves.

Figure 12 shows the transient contour of the peak value in the wall-normal direction of u' and the contour of the amplitude of u' for traveling crossflow waves obtained by DNS. Its distribution
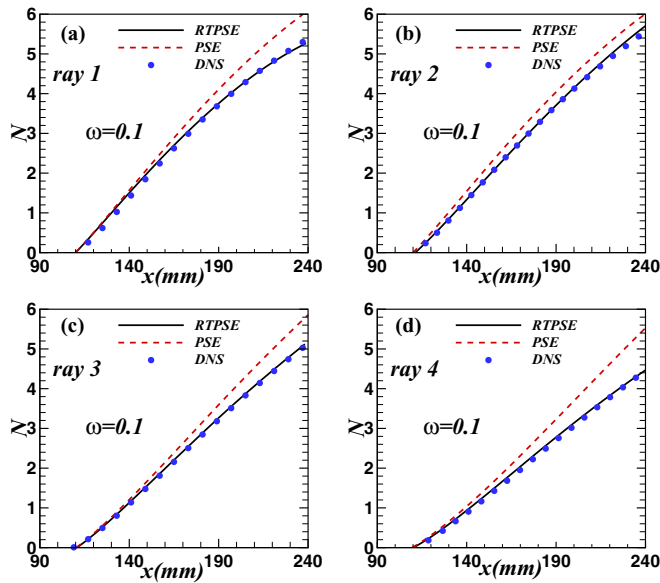

FIG. 15. Comparison of the amplitude ratio $N = \ln(A/A_{x=110})$ among RTPSE, PSE, and DNS for traveling crossflow waves: (a) ray 1, (b) ray 2, (c) ray 3, and (d) ray 4.
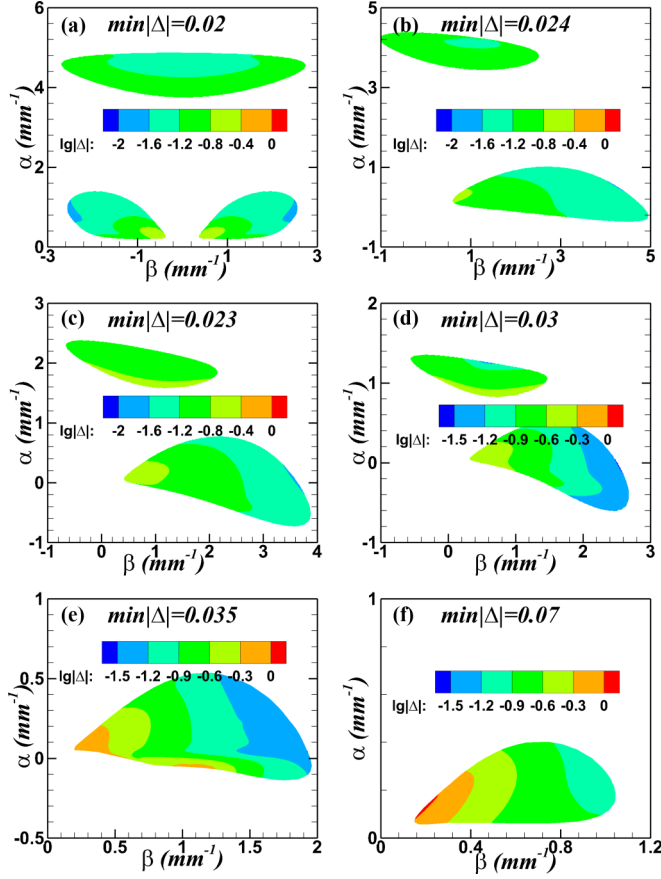
FIG. 16. Analysis of the caustics condition by contours of $lg|\Delta|$ at $x = 200$ mm for different ϕ: (a) $\phi = 0°$, (b) $\phi = 30°$, (c) $\phi = 60°$, (d) $\phi = 90°$, (e) $\phi = 120°$, and (f) $\phi = 150°$.

characteristics is similar to that of stationary crossflow waves, except that the inclination angle of the ribbon is large and the maximum amplitude is about twice that of the latter.

Figure 13 presents the evolution path of traveling crossflow waves obtained by DNS and RT. Compared with the result of stationary crossflow waves, a better agreement between the tracing ray 2 by RT and the evolution path by DNS is obtained, indicating that the tracing ray is a good option to analyze the disturbance evolution in 3D boundary layers for traveling crossflow waves. Furthermore, the angle ϕ_p of traveling crossflow waves is smaller than that of stationary crossflow waves, implying that the location of the beginning transition for traveling crossflow waves is farther from the leeward of the blunt cone than for the stationary crossflow waves.

Figures 14 and 15 show the comparison of the azimuthal wave number n and the amplitude ratio obtained by RTPSE, PSE, and DNS along four tracing rays for traveling crossflow waves, respectively. The results show that the symbols for both the azimuthal wave number and the amplitude ratio obtained by DNS are overlapped with the lines predicted by RTPSE, while there is a clear gap between the results by DNS and by PSE, indicating that the evolution of traveling crossflow waves can be predicted by RTPSE very well and that the traditional PSE could not predict this evolution well. Compared with the result for stationary crossflow waves, RTPSE has a better prediction for traveling crossflow waves. Furthermore, the traditional PSE overpredicts the amplitude of traveling crossflow waves for all four tracing rays, while the relationship between the amplitude of stationary crossflow waves predicted by the traditional PSE and that by DNS depends

on the tracing ray, which may cause a false impression that the traditional PSE can predict the amplitude of stationary crossflow waves for a special tracing ray.

D. Validation of the application condition for RT

As mentioned in Sec. II, RT is invalid near a caustic with the caustic condition $\Delta = 0$ in Eq. (24). Hence, this condition needs to be validated for the blunt cone model. Because Δ is a complex number due to the complex dispersion relation in Eq. (8), we check the module of Δ, namely, $|\Delta|$, for all unstable waves at different positions ϕ with a given $x = 200$ mm, and the results of only six positions are shown in Fig. 16. As shown in Fig. 16(a), the unstable area of the second Mack mode instability (upper branch) and the first Mack mode instability (lower branch) is symmetric with the symmetry axis $\beta = 0$ because the basic flow profile in this position has no crossflow velocity and has the same characteristic as the basic flow profile on a flat plate. As ϕ increases, as shown in Figs. 16(b)–16(f), the symmetry is broken down, and the unstable area of the second Mack mode instability decreases and disappears at $\phi = 120°$, while the stationary crossflow instability begins to appear at $\phi = 30°$. In all positions, the minimum value of $|\Delta|$ is about 0.02, which is in the same order as the growth rate of the disturbance, implying that the caustic condition does not occur at $x = 200$ mm for all unstable waves. Because the basic flow profiles are similar in most areas of the model except the area near the leeward and the nose tip [19], the caustics condition also does not occur for all unstable waves on the blunt cone with an AoA, and as a result the caustics condition would not exist for 3D compressible boundary layers.

V. SUMMARY AND CONCLUSIONS

In this paper, we propose a method, namely, RTPSE, to predict the linear evolution of disturbances in 3D boundary layers. The presented method contains two major improvements compared with the conventional PSE: (1) the marching line is along the group velocity direction, and (2) the variation of the spanwise wave number is predicted by RT. Compared with the previous methods, RTPSE can address stationary crossflow waves and traveling crossflow waves. To validate our method, the linear evolution of stationary and traveling crossflow disturbances is performed by DNS. The spanwise wave number predicted by RT coincides with that by DNS, and the amplitude ratio calculated by RTPSE is in good agreement with that by DNS for the whole wave packet. In addition, the application condition of RT is investigated numerically, and the caustics do not occur for unstable disturbances, implying that RT is valid. Therefore, RTPSE makes it possible to accurately predict the linear evolution of disturbances in 3D boundary layers.

[1] D. Arnal and G. Casalis, Laminar-turbulent transition prediction in three-dimensional flows, Prog. Aerosp. Sci. **36**, 173 (2000).

[2] H. L. Reed, W. S. Saric, and D. Arnal, Linear stability theory applied to boundary layers, Annu. Rev. Fluid Mech. **28**, 389 (1996).

[3] T. Herbert, Parabolized stability equations, Annu. Rev. Fluid Mech. **29**, 245 (1997).

[4] E. Reshotko, Boundary-layer stability and transition, Annu. Rev. Fluid Mech. **8**, 311 (1976).

[5] M. Gaster, On the effects of boundary-layer growth on flow stability, J. Fluid Mech. **66**, 465 (1974).

[6] Z. Huang and X. Wu, A non-perturbative approach to spatial instability of weakly non-parallel shear flows, Phys. Fluids **27**, 054102 (2015).

[7] Z. Huang and X. Wu, A local scattering approach for the effects of abrupt changes on boundary-layer instability and transition: A finite-Reynolds-number formulation for isolated distortions, J. Fluid Mech. **822**, 444 (2017).

[8] T. Cebeci and K. Stewartson, On stability and transition of three-dimensional flows, AIAA J. **18**, 398 (1980).

[9] M. Malik and P. Balakumar, Instability and transition in three-dimensional supersonic boundary layers, in *4th Symposium on Multidisciplinary Analysis and Optimization* (AIAA, Reston, 1992), Paper No. 1992–5049.

[10] C. Su and H. Zhou, Transition prediction for supersonic and hypersonic boundary layers on a cone with angle of attack, Sci. China Ser. G: Phys. Mech. Astron. **52**, 1223 (2009).

[11] F. Li, M. Choudhari, and C. L. Chang, Stability analysis for HIFiRE experiments, in *42nd AIAA Fluid Dynamics Conference and Exhibit* (AIAA, Reston, 2012), Paper No. 2012–2961.

[12] A. H. Nayfeh, Stability of three-dimensional boundary layers, AIAA J. **18**, 406 (1980).

[13] R. Song, L. Zhao, and Z. Huang, Conservation relation of generalized growth rate in boundary layers, Appl. Math. Mech-Engl. **39**, 1755 (2018).

[14] J. Lighthill, *Waves in Fluids* (Cambridge University, Cambridge, England, 1978), pp. 385–399.

[15] V. Citro and P. Luchini, Multiple-scale approximation of instabilities in unsteady boundary layers, Eur. J. Mech B-Fluid. **50**, 1 (2015).

[16] L. Zhao, G. Yu, and J. Luo, Extension of eN method to general three-dimensional boundary layers, Appl. Math. Mech.-Engl. **38**, 1007 (2017).

[17] F. P. Bertolotti and T. Herbert, Analysis of the linear stability of compressible boundary layers using the PSE, Theor. Comp. Fluid Dyn. **3**, 117 (1991).

[18] F. P. Bertolotti, T. Herbert, and P. R. Spalart, Linear and nonlinear stability of the Blasius boundary layer, J. Fluid Mech. **242**, 441 (1992).

[19] P. Balakumar and M. A. Kegerise, Receptivity of hypersonic boundary layers over straight and flared cones, AIAA J. **53**, 2097 (2015).

[20] C. L. Chang, LASTRAC.3d: Transition Prediction in 3D Boundary Layers, in *34th AIAA Fluid Dynamics Conference and Exhibit* (AIAA, Reston, 2004), Paper No. 2004–2542.

[21] A. Moyes, P. Paredes, T. Kocian, and H. L. Reed, Secondary instability analysis of crossflow on a hypersonic yawed straight circular cone, J. Fluid Mech. **812**, 370 (2017).

[22] N. D. Tullio, P. Paredes, N. D. Sandham, and V. Theofilis, Laminar-turbulent transition induced by a discrete roughness element in a supersonic boundary layer, J. Fluid Mech. **735**, 613 (2013).

[23] J. Liu, S. Zhang, and S. Fu, Linear spatial instability analysis in 3D boundary layers using plane-marching 3D-LPSE, Appl. Math. Mech.-Engl. **37**, 1013 (2016).

[24] T. Herbert, On the stability of 3D boundary layers, in *28th Fluid Dynamics Conference* (AIAA, Reston, 1997), Paper No. 1997–1961.

[25] T. S. Kocian, A. J. Moyes, H. L. Reed, S. A. Craig, W. S. Saric, S. P. Schneider, and J. B. Edelman, Hypersonic crossflow instability, J. Spacecraft Rockets **56**, 432 (2019).

[26] D. J. Dinzl and G. V. Candler, Direct simulation of hypersonic crossflow instability on an elliptic cone, AIAA J. **55**, 1769 (2017).

[27] P. Balakumar and L. Owens, Stability of Hypersonic Boundary Layers on a Cone at an Angle of Attack, in *40th Fluid Dynamics Conference and Exhibit* (AIAA, Reston, 2010), Paper No. 2010–4718.

[28] N. Oliviero, EPIC: A new and advanced nonlinear parabolized stability equation solver, Master's thesis, Texas A&M University, 2015.

[29] R. Courant and D. Hilbert, *Methods for Mathematical Physics* (Wiley-Interscience, New York, 1962), pp. 97–103.

[30] G. B. Whitham, Group velocity and energy propagation for three-dimensional waves, Comm. Pure Appl. Math. **14**, 675 (1961).

[31] M. Gaster, The development of three-dimensional wave packets in a boundary layer, J. Fluid Mech. **32**, 173 (1968).

[32] R. J. Lingwood, On the application of the Briggs' and steepest-descent methods to a boundary-layer flow, Stud. Appl. Math. **98**, 213 (1997).

[33] M. J. Taylor and N. Peake, The long-time behaviour of incompressible swept-wing boundary layers subject to impulsive forcing, J. Fluid Mech. **355**, 359 (1998).

[34] T. J. Juliano, R. L. Kimmel, S. Willems, A. Guelhan, and S. P. Schneider, HIFiRE-1 Surface Pressure Fluctuations from High Reynolds, High Angle Ground Test, in *52nd Aerospace Sciences Meeting* (AIAA, Reston, 2014), Paper No. 2014–0429.

[35] L. Zhao, C. Zhang, J. Liu, and J. Luo, Improved algorithm for solving nonlinear parabolized stability equations, Chinese Phys. B **25**, 84701 (2016).

[36] L. Zhao, M. Dong, and Y. Yang, Harmonic linearized Navier-Stokes equation on describing the effect of surface roughness on hypersonic boundary-layer transition, Phys. Fluids **31**, 034108 (2019).

[37] G. S. Jiang and C. W. Shu, Efficient implementation of weighted ENO schemes, J. Comput. Phys. **126**, 202 (1996).

[38] X. Zhong and Y. Ma, Boundary-layer receptivity of Mach 7.99 flow over a blunt cone to free-stream acoustic waves, J. Fluid Mech. **556**, 55 (2006).

[39] F. Li, M. Choudhari, P. Paredes, and L. Duan, High-frequency instabilities of stationary crossflow vortices in a hypersonic boundary layer, Phys. Rev. Fluids **1**, 053603 (2016).

[40] M. Kloker, U. Konzelmann, and H. Fasel, Outflow boundary conditions for spatial Navier-Stokes simulations of transition boundary layers, AIAA J. **31**, 620 (1993).

[41] Z. Huang, W. Cao, and H. Zhou, The mechanism of breakdown in laminar-turbulent transition of a supersonic boundary layer on a flat plate: Temporal mode, Sci. China Ser. G: Phys. Mech. Astron. **48**, 614 (2005).